

On-The-Fly Observing System of the Nobeyama 45-m and ASTE 10-m Telescopes

Tsuyoshi SAWADA¹, Norio IKEDA^{1,2,3}, Kazuyoshi SUNADA^{1,4}, Nario KUNO¹, Takeshi KAMAZAKI⁵, Koh-Ichiro MORITA^{1,5}, Yasutaka KURONO^{1,6}, Norikazu KOURA⁷, Katsumi ABE⁷, Sachiko KAWASE⁷, Jun MAEKAWA⁸, Osamu HORIGOME⁹, and Kiyohiko YANAGISAWA⁹

¹*Nobeyama Radio Observatory, National Astronomical Observatory,
462-2 Nobeyama, Minamimaki, Minamisaku, Nagano 384-1305
sawada@nro.nao.ac.jp*

²*Institute of Space and Astronautical Science, Japan Aerospace Exploration Agency,
Yoshinodai 3-1-1, Sagami-hara, Kanagawa 229-8510*

³*Department of Astronomical Science, Graduate University for Advanced Studies, 2-21-1 Osawa, Mitaka, Tokyo 181-8588*

⁴*Mizusawa VERA Observatory, National Astronomical Observatory, 2-12 Hoshigaoka, Mizusawa, Oshu, Iwate 023-0861*

⁵*ALMA-J Project Office, National Astronomical Observatory, 2-21-1 Osawa, Mitaka, Tokyo 181-8588*

⁶*Department of Astronomy, Graduate School of Science, The University of Tokyo, 7-3-1 Hongo, Bunkyo, Tokyo 113-0033*

⁷*Fujitsu Ltd., 1-9-3 Nakase, Mihama, Chiba, Chiba 261-8588*

⁸*Maekawa Co., Ltd., 8240-6078 Nishi-Ide, Oizumi, Hokuto, Yamanashi 409-1501*

⁹*Fujitsu Nagano Systems Engineering Ltd., 1415 Tsurugamidoricho, Nagano, Nagano 380-0813*

(Received 2007 October 22; accepted 2007 November 30)

Abstract

We have developed spectral line On-The-Fly (OTF) observing mode for the Nobeyama Radio Observatory 45-m and the Atacama Submillimeter Telescope Experiment 10-m telescopes. Sets of digital autocorrelation spectrometers are available for OTF with heterodyne receivers mounted on the telescopes, including the focal-plane 5×5 array receiver, BEARS, on the 45-m. During OTF observations, the antenna is continuously driven to cover the mapped region rapidly, resulting in high observing efficiency and accuracy. Pointing of the antenna and readouts from the spectrometer are recorded as fast as 0.1 second. In this paper we report improvements made on software and instruments, requirements and optimization of observing parameters, data reduction process, and verification of the system. It is confirmed that, using optimal parameters, the OTF is about twice as efficient as conventional position-switch observing method.

Key words: radio lines: ISM — techniques: image processing — telescopes

1. Introduction

On-The-Fly (OTF) is a technique to perform mapping observations efficiently with single-dish radio telescopes. In OTF, the antenna is driven continuously in a region to be mapped and the data are taken in a short interval, instead of integrating at discrete positions on the sky (such a conventional “step-and-integrate” method is hereafter referred to as *position-switch* [PSW] observation). OTF observations have advantages over PSW modes as follows: (1) Observing efficiency improves since dead time of the telescope is reduced and a large number ($\gtrsim 10^2$) of on-source integrations are made per an emission-free reference integration; (2) The system variation (e.g., atmospheric conditions, receiver gain, pointing of the telescope) less affects the map since the entire map can be covered in a short period; and (3) Since the data are acquired more frequently than the Nyquist sampling rate, the spatial information is not lost. Comprehensive review and discussion on OTF technique have been made by Mangum, Emerson, & Greisen (2007).

OTF technique has been commonly and widely used in radio continuum observations. Technical limitations,

such as fast readout from the spectrometer and dealing with huge data, had prevented OTF from being applied to spectral line observations. In the last decade spectral line OTF has been made practicable in some observatories (e.g., Mangum, Emerson, & Greisen 2000; Muders et al. 2000; Ungerechts et al. 2000) and is established as an efficient method. Likewise, with the Nobeyama Radio Observatory (NRO) 45-m and Atacama Submillimeter Telescope Experiment (ASTE¹: Ezawa et al. 2004; Kohno 2005) 10-m telescopes, continuum OTF observations have already been available. We enabled the telescopes to be operated in OTF observing mode, as reported in this paper. The OTF observing system of the telescopes now works with an array of digital autocorrelation spectrometers (MAC; Sorai et al. 2000). Heterodyne receivers equipped with the telescopes, including the 25-beam focal plane array receiver (BEARS: Sunada et al. 2000; Yamaguchi et al. 2000) on the 45-m telescope, can

¹ The ASTE project is driven by NRO, a branch of National Astronomical Observatory of Japan, in collaboration with University of Chile, and Japanese institutes including University of Tokyo, Nagoya University, Osaka Prefecture University, Ibaraki University, and Kobe University.

be connected to the MAC and be available for OTF observations.

The capability of OTF to obtain a high-quality map efficiently is important in various scientific fields. For example, investigating how the initial mass function (IMF) of stars is determined is one of the most important issues in astronomy. Recent studies have suggested that the stellar IMF is well related to the mass function (MF) of dense molecular cloud cores (e.g., Ikeda, Sunada, & Kitamura 2007), which are sites of star formation. Therefore detecting a number of cores in various star forming regions is needed in order to study the relation between star-forming activity and MF or physical/dynamical conditions of the cores. In this case sensitive unbiased mapping observations of wide fields are required. In addition, OTF data are ideal to be combined with interferometric data, since they preserve spatial information in the (spatially) low frequency regime, which is lost via interferometric observations. Thus, the fidelity of high resolution images of, e.g., molecular cloud cores or external galaxies, taken with interferometers are significantly improved by being combined with OTF data. The fidelity (preserving total flux) is essential to various kinds of studies. For instance, in order to investigate the evolution of the interstellar medium (formation and destruction of giant molecular cloud associations [GMAs]) across spiral arms in external galaxies, it is required to detect not only GMAs, which are spatially confined to spiral arms, but also diffuse emission in interarm regions.

In order to make spectral line OTF observations available with the NRO 45-m and the ASTE 10-m telescopes, various improvements have been applied to the control software system, COSMOS-3 (Morita et al. 2003; Kamazaki et al. 2005), and related instruments. In particular, fast and synchronized control of instruments and handling of huge amount of data are the difficulties, as discussed later. The way to determine optimal observing parameters is also complicated.

In this paper we report practical information and implementation of the OTF observing mode for the telescopes. Basic concepts and parameters of OTF observations are introduced in §2, followed by a brief description on controls of related instruments in §3. Requirements on observing parameters, procedures to estimate sensitivity, and how to maximize observing efficiency are explained in §4. We describe the data reduction process in §5. Desired characteristics of convolution functions to regrid the data onto a map are discussed and some appropriate functions are shown. In §6 we describe the measurements of driving performance of the antennas, comparison with PSW map, and verification of frequency-switch observing mode.

2. Basic Observing Process and Parameters

An OTF scan pattern is schematically illustrated in Fig. 1. A constant-speed raster scan with a single-beam receiver is assumed. Like usual PSW observations, the standard “chopper-wheel” technique (Penzias & Burrus 1973; Ulich & Haas 1976) is employed to calibrate the

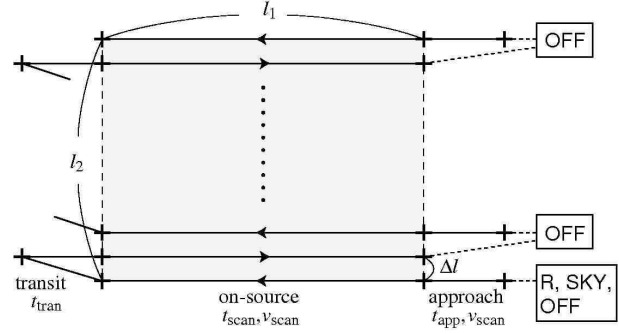


Fig. 1. An example of scan pattern of OTF observations. The gray rectangle is a region to be mapped with a set of horizontal scans. The case of $N_{\text{scan}}^{\text{SEQ}} = 2$ (an OFF is inserted before every 2 ON scans) is shown.

antenna temperature T_A^* in which the atmospheric and antenna losses are corrected. For the chopper-wheel calibration, a hot load (R) at the ambient temperature and blank sky (SKY) are observed during the observation in an appropriate interval. Data at an emission-free reference position (OFF) are taken before every on-source scan (ON, hereafter simply “scan”) or set of several scans. The OFF is usually taken by pointing the antenna outside the source. However it can also be taken by shifting observing frequency (see §3.4.2).

During the scan the antenna is driven at a constant speed (v_{scan}) on the sky and the data are “dumped” from the spectrometer at an interval of t_{dump} . The “approach-run” at a speed v_{scan} is inserted before every scan to let the antenna move stably during the scan. If there is no OFF between two scans, a “transit-run” (from the end point of the scan to the start point of the next approach-run) is inserted.

We set fundamental parameters as follows (see Fig. 1). In §4 we discuss how to determine them. The dimension of the mapping area is $l_1 \times l_2$ (l_1 along the scan, l_2 across the scan). The scan speed of the antenna on the sky is v_{scan} . Time to be taken in an approach-run, a main (on-source) scan, and a transit-run are t_{app} , $t_{\text{scan}} = l_1/v_{\text{scan}}$, and t_{tran} , respectively. A separation between the scan rows is Δl , the number of scans taken between a pair of OFFs is $N_{\text{scan}}^{\text{SEQ}}$, and the grid spacing of a map to be made is d . Time to be taken to slew the antenna between the mapped region and the OFF position is $t_{\text{tran}}^{\text{OFF}}$. The parameters t_{app} , t_{tran} , and $t_{\text{tran}}^{\text{OFF}}$ depend on the performance of the antenna, the scan speed v_{scan} , position on the sky, etc., and are typically in the range of a few to 10 seconds. Measurements of the performance of the antenna are described in §6.1. The time interval between each dump from the spectrometer is t_{dump} .

3. Control of Related Instruments

In OTF, spectral data are dumped at short interval (~ 0.1 second) while the antenna is continuously driven across the sky. Consequently the following difficulties arise.

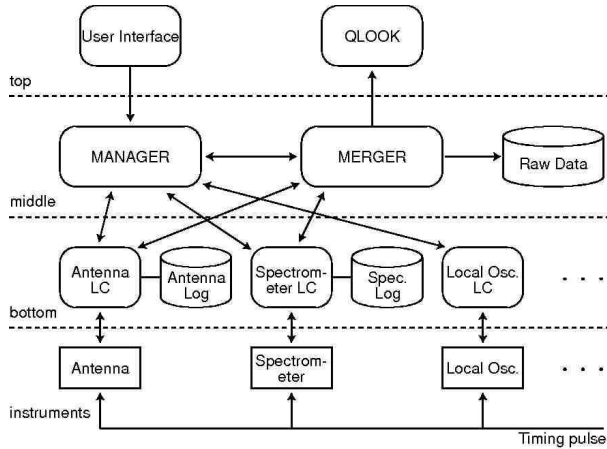


Fig. 2. Schematic illustration of three-layered COSMOS-3 architecture. Rounded rectangles are components of COSMOS-3, cylinder symbols are data storage and files therein, and rectangles are individual instruments.

Antenna. The antenna should be smoothly driven on a scan path. The sky coordinates, toward which the antenna pointed, have to be recorded for each data dump.

Spectrometer. Data dump is done at short interval, and it must be synchronized with the antenna driving.

Local oscillator. Doppler correction of the telescope with respect to a rest frame and frequency switch (FSW) are difficult to be implemented in a conventional way, since exceedingly rapid control of the frequency is required.

Data production and storage. High data production rate, caused by the fact that the data are dumped $\sim 10^2$ times more frequently than typical PSW observations, may cause trouble on data storage and reduction process.

In this section we describe the control system and instruments to resolve these issues.

3.1. COSMOS-3

The control software system of the telescopes is COSMOS-3 (Morita et al. 2003). It is designed to have a three-layer architecture, as illustrated in Fig. 2. The interface with observers is provided in the top layer. In the middle layer, MANAGER and MERGER exist. The MANAGER controls the observation by receiving instruction from observers and interacting with Local Controllers (LCs), which directly control instruments, in the bottom layer. The MERGER receives outputs from LCs and produces calibrated data. The observer can view a Quick Look (QLOOK) of the data and check if the observation is running properly. Synchronization of instruments with each other is managed with 1, 10, 50, and 100-Hz timing pulses, which are generated and distributed from the standard clock system of the observatory.

3.2. Antenna

Before every approach-run, the antenna LC instructs the antenna to settle on the starting point of the approach-run. When the antenna is judged to be steady (the positional error has been within a tolerance for a specified duration), the MANAGER decides the timing and coordinates of the following approach-run(s), scan(s), and transit-run(s). The antenna LC instructs the antenna to follow an ideal scan path at the decided timing. The ideal coordinates, toward which the antenna is desired to point, is hereafter called PROG values. The PROG values for every 0.1 second are calculated and transmitted to the antenna, 0.2 second before it is used. The antenna manages the timing to use the transmitted coordinates with the 10-Hz (0.1-second) timing signal. Two neighboring PROG values are linearly interpolated. The antenna is driven to follow the interpolated positions, referring the 50 and 100-Hz timing signals.

Meanwhile, the actual pointing of the antenna (hereafter referred to as REAL values) jitters around the PROG values. The amount of the jitter ($\text{PROG} - \text{REAL}$) is measured, in case of the 45-m telescope, using the encoder readout of the master collimator and the pointing deviation between the master collimator and the main reflector. In case of the 10-m telescope, the encoder readout of the antenna is used. The PROG (in both equatorial and horizontal coordinates) and $\text{PROG} - \text{REAL}$ (horizontal coordinates) values are both written onto a file, the *Antenna Log* file, along with time stamps at every 0.1 second.

3.3. Spectrometer

It is essential to synchronize the timing of data acquisition with that of the antenna driving, particularly in case of OTF, since the data dump time is very short. The timing is managed as follows.

When an observation starts, observing parameters, such as interval of data dumps (0.1 second) and number of datasets to be dumped, are calculated by the MANAGER from instructions made by the observer. They are sent to the spectrometer LC and then to the spectrometer, in advance of data acquisition. For each scan, the MANAGER decides the time to start the scan as mentioned above. The LC is informed of the time, waits until 1 second before it, and then sends a command to the spectrometer to start integration. After receiving it, the spectrometer begins to acquire the data, triggered by the next fall-down of the 1-Hz, 50%-duty timing pulse. It dumps the data at every 0.1 second during the scan.

Though the spectrometer outputs datasets at every 0.1 second, observers can specify t_{dump} to be $0.1N$ ($N = 1, 2, \dots$) seconds to reduce the data size. Every 0.1-second output is transferred to the LC. The LC averages successive N datasets if $N > 1$, and writes them down onto a file (the *Spectrometer Log* file) along with time stamps.

3.4. Local Oscillator

3.4.1. Doppler Tracking

When a wide area is mapped, the radial velocity of the telescope (v_{rad}) with respect to the reference frame (e.g., the Local Standard of Rest [LSR]) significantly changes from point to point: the velocity gradient across the sky plane amounts to roughly $0.8 \text{ km s}^{-1} \text{ deg}^{-1}$ (LSR) at maximum in NRO. In PSW observations, the radial velocity of the telescope at each position is calculated and the local oscillator (LO) frequency is shifted before the integration starts, in order to track the Doppler shift caused by Δv_{rad} .

However, in OTF observations, the antenna runs on a scan path (thus v_{rad} gradually changes), and during which the spectral data are continuously taken at a short interval. In this case it is difficult to track v_{rad} by shifting the LO frequency continuously during the scan. Therefore we do not make any shift on LO frequency during the OTF scans. Instead, the Doppler correction is carried out by software: in the production process of spectral data (MERGER; see below), v_{rad} for each ON integration is calculated, and then channel shift operation is made.

3.4.2. Frequency Switching

When spatially-widespread and/or narrow lines (e.g., CO in nearby molecular clouds) are mapped, FSW observing technique has been widely used. Conventional FSW observations with the NRO 45-m and ASTE 10-m telescopes are performed as follows. The LO frequency is switched between the original value ν_{LO}^0 and slightly shifted value $\nu_{\text{LO}}^0 \pm \Delta \nu_{\text{LO}}$. The switching cycle is in the order of $\sim 1 \text{ Hz}$, and the frequency throw $\Delta \nu_{\text{LO}}$ is typically several MHz. The averager/integrator of the spectrometer behaves in adding and subtracting mode, synchronized with the frequency shift of the LO, during the ON integration (the averager/integrator does nothing during a margin for the transition of frequency). Thus the ON concurrently plays a role of OFF. Accordingly the original signal and a negative-amplitude signal appear on the spectrum at a separation of $\Delta \nu_{\text{LO}}$. The final spectrum is demodulated by invert, shift and add operation.

In OTF, the difficulty of shifting LO frequency during a short integration again arises. We have implemented FSW observing mode in OTF by shifting the LO frequency at OFF position only: ν_{LO}^0 is used during ON, while $\nu_{\text{LO}}^0 \pm \Delta \nu_{\text{LO}}$ is used during OFF. The emission line existing (if any) at OFF position shifts by $\Delta \nu_{\text{LO}}$, thus it can be virtually regarded as emission-free reference.

3.5. Spectral Data Production

As described above, the antenna pointings are recorded in the Antenna Log file at every 0.1 second, and the readouts from the spectrometer are written onto the Spectrometer Log file at every $0.1N$ seconds. The MERGER, which is a process to produce spectral data files, runs during the observation (it can also be executed asynchronously after the observation). The MERGER process reads the Spectrometer Log file, calculates the standard chopper-wheel equation to calibrate the antenna temperature, and shifts the resultant spectra along the fre-

quency channels to correct Doppler shift. The MERGER also reads the Antenna Log file. By comparing time stamps written in both log files, it calculates sky coordinates, toward which the antenna was actually pointed at the moment of each dump, using the PROG (equatorial) and PROG – REAL (horizontal) values. The derived coordinates are written in the header of the spectral data file. In this way intensity- and velocity-calibrated spectra are written on a file, called the *Raw Data* file.

In practical implementation, the trouble with the Raw Data is their large sizes. If the 25-beam, 1024-channel data are represented as 32-bit and dumped every 0.1 second, the data rate goes up to $\simeq 3.5 \text{ GB hour}^{-1}$ (data headers are neglected). In order to reduce the size of the Raw Data, the quantization level, Q [bit], must be as small as possible. When the peak antenna temperature of the intrinsic spectrum is T_p and rms noise is σ , observed antenna temperature between the minimum ($-N\sigma$; $N \simeq 3$) and maximum ($T_p + N\sigma$) is quantized into 2^Q levels. The quantization noise is roughly written as $\sigma_Q = (T_p + 2N\sigma)/2^{Q+1}$. Since the noise level increases to $\sqrt{\sigma^2 + \sigma_Q^2}$, the overhead in the observing time (the ratio between Q -bit and ∞ -bit cases) is

$$\frac{t_Q}{t_\infty} = 1 + \left(\frac{T_p + 2N\sigma}{2^{Q+1}\sigma} \right)^2, \quad (1)$$

meaning that the loss increases when the signal-to-noise ratio of individual spectrum, T_p/σ , is high. Supposing an extreme case for the current system: peak antenna temperature $T_p = 100 \text{ [K]}$, system noise temperature $T_{\text{sys}} = 100 \text{ [K]}$, frequency resolution $B = 1 \text{ [MHz]}$, and data dump time $t_{\text{dump}} = 0.1 \text{ [s]}$, we obtain $t_Q/t_\infty - 1 \simeq (320/2^{Q+1})^2$. For $Q = 8, 12$, and 16 , $t_Q/t_\infty - 1$ becomes 0.40 , 1.5×10^{-3} , and 6.1×10^{-6} , respectively. We adopted $Q = 12$ (4096 levels), for which the quantization noise is practically negligible, resulting in the maximum data rate of $\simeq 1.3 \text{ GB hour}^{-1}$.

In addition, the MERGER supports options of channel trimming and channel binning. When these options are specified by the observer, the MERGER trims and/or bins up channels of the spectra before writing them down on the Raw Data file.

It should be noted that the 12-bit quantization may affect the data in the following situation: bandpass becomes nearly 0 (i.e., T_A^* diverges) at the band edges, or an extremely intense spurious signal appears. The observer should pay attention to the obtained spectra through QLOOK. This problem can be evaded by trimming the band edges and/or spurious signals, since the data are quantized *after* the trim.

4. Observing Parameters

4.1. Requirements on Sampling

As a result of an observation, the mapped region is filled with data points. The data sampling separation is $v_{\text{scan}} t_{\text{dump}}$ along the scan, Δl across the scan. Mangum, Emerson, & Greisen (2007) discussed requirements on

the sampling, as summarized as follows. It is requested that, at least, the sampling rates $v_{\text{scan}}t_{\text{dump}}$ and Δl are both more frequent than the Nyquist sampling rate $\lambda/2D$, where λ is the observed wavelength and D is the diameter of the antenna aperture. In case of $\lambda = 2.6$ mm (115 GHz) observations with the 45-m telescope $\lambda/2D \simeq 6''$, which corresponds to $\simeq 1/2.5$ of the half-power beam width (HPBW). Practically a sampling more frequent than the Nyquist rate is required to avoid aliasing noise and beam smearing effects. Since the data points do not align on any regular grid due to the antenna jitter etc., the data should be regridded onto a regular grid using a gridding convolution function (GCF) in the data reduction process (see §5).

4.2. Estimation of Sensitivity

We estimate the sensitivity of a single-beam observation. Application to a multi-beam receiver is discussed later.

The total number of scan rows in an observation is $N_{\text{row}} = l_2/\Delta l + 1$. The total on-source integration time becomes

$$t_{\text{tot}}^{\text{ON}} = N_{\text{row}} t_{\text{scan}}. \quad (2)$$

The total time spent to run an observation including R, SKY, OFF, antenna slew, etc. is estimated to be

$$t_{\text{tot}}^{\text{OBS}} = N_{\text{row}} \left(t_{\text{scan}} + t_{\text{OH}} + \frac{t_{\text{OFF}}}{N_{\text{scan}}^{\text{SEQ}}} \right) f_{\text{cal}}, \quad (3)$$

where t_{OFF} is an integration time for an OFF, and f_{cal} is an overhead of R-SKY calibration (if 1 minute is consumed to obtain R and SKY data at every 15 minutes, $f_{\text{cal}} = 16/15$). The t_{OH} is an overhead time per one scan row, which consists of go-and-return to the OFF point $2t_{\text{tran}}^{\text{OFF}}$, time for approach- and transit-run t_{app} and t_{tran} , thus is written as

$$t_{\text{OH}} = \frac{2t_{\text{tran}}^{\text{OFF}}}{N_{\text{scan}}^{\text{SEQ}}} + t_{\text{app}} + \frac{N_{\text{scan}}^{\text{SEQ}} - 1}{N_{\text{scan}}^{\text{SEQ}}} t_{\text{tran}}. \quad (4)$$

The $t_{\text{tran}}^{\text{OFF}}$ depends on the distance between the mapped region and the OFF position; t_{app} and t_{tran} should be chosen so that the antenna follows the PROG position during the scans. Now the ratio of on-source time to the total time spent is

$$\eta_{\text{ON/OBS}} = \frac{t_{\text{tot}}^{\text{ON}}}{t_{\text{tot}}^{\text{OBS}}} \quad (5)$$

$$= \frac{t_{\text{scan}}}{t_{\text{scan}} + t_{\text{OH}} + t_{\text{OFF}}/N_{\text{scan}}^{\text{SEQ}}} \cdot \frac{1}{f_{\text{cal}}}. \quad (6)$$

The total on-source integration time for a map grid point, $t_{\text{cell}}^{\text{ON}}$, is a sum of time during which the beam scans within the grid cell. Since the data are convolved using a GCF to construct a regularly gridded map, effectively a factor η is multiplied:

$$t_{\text{cell}}^{\text{ON}} = \eta \cdot \frac{d^2}{l_1 l_2} t_{\text{tot}}^{\text{ON}} \quad (7)$$

$$\simeq \frac{\eta t_{\text{scan}} d^2}{l_1 \Delta l}. \quad (8)$$

The factor η is a constant determined by the extent of the used GCF and is calculated as follows. Suppose that observed points $i = 1, 2, \dots$ are uniformly distributed around the grid point and each point has a spectrum $T_i(k)$ ($k = 1, \dots, N_{\text{CH}}$), rms noise temperature σ_i , and a GCF weight w_i . We assume that the on-source integration time t_0 and therefore the rms noise temperature $\sigma_i = \sigma_0 = T_{\text{sys}}/(\eta_q \sqrt{B} t_0)$ of each point are both constant. Here T_{sys} is the system noise temperature, B is the frequency resolution of the spectra, and η_q is the quantization efficiency of the spectrometer. In case of MAC $\eta_q = 0.88$; and hereafter η_q is omitted from expressions. The convolved spectrum $T(k)$ is written as $T = (\sum w_i T_i)/(\sum w_i)$, and its noise temperature σ becomes $\sigma = (\sqrt{\sum w_i^2}/\sum w_i) \sigma_0 = T_{\text{sys}}/\sqrt{B t_{\text{cell}}^{\text{ON}}}$, where $t_{\text{cell}}^{\text{ON}} \equiv t_0 (\sum w_i)^2 / \sum (w_i^2)$. If we take the grid spacing as the unit of spatial length and re-define t_0 as the on-source integration time per unit area (1 grid cell), summations can be rewritten with integrals: $t_{\text{cell}}^{\text{ON}} = t_0 (\int w dx dy)^2 / \int w^2 dx dy \equiv \eta t_0$. Approximate values of η for GCFs Bessel \times Gauss, Sinc \times Gauss, Gauss, Pillbox, and Spheroidal (see §5) with default parameters are, respectively, 4.3, 1.2, 6.3, 1.0, and 10.

Redefining B as the frequency resolution of a *map* to be made, the noise of the map due to on-source integration is estimated to be

$$\Delta T_A^*(\text{ON}) = \frac{T_{\text{sys}}}{\sqrt{B t_{\text{cell}}^{\text{ON}}}}, \quad (9)$$

the standard radiometer equation. On the other hand, the number of OFF points used to consist a map grid point is roughly written as $d/\Delta l$ (here the extent of the GCF is neglected). Thus the effective OFF integration time for a grid cell is

$$t_{\text{cell}}^{\text{OFF}} \simeq \frac{d}{\Delta l} t_{\text{OFF}}, \quad (10)$$

and the noise due to OFF points becomes

$$\Delta T_A^*(\text{OFF}) = \frac{T_{\text{sys}}}{\sqrt{B t_{\text{cell}}^{\text{OFF}}}}. \quad (11)$$

Therefore the total noise level of the map is written as

$$\Delta T_A^* = \sqrt{\Delta T_A^*(\text{ON})^2 + \Delta T_A^*(\text{OFF})^2} \quad (12)$$

$$= \frac{T_{\text{sys}}}{\sqrt{B}} \sqrt{\frac{1}{t_{\text{cell}}^{\text{ON}}} + \frac{1}{t_{\text{cell}}^{\text{OFF}}}}. \quad (13)$$

Validity of this equation has been practically confirmed (see §6.2).

4.3. Optimization

The noise level of a map achieved in unit observing time $\Delta T_A^*(0)$ is written as

$$\Delta T_A^*(0) = \Delta T_A^* \sqrt{t_{\text{tot}}^{\text{OBS}}} \quad (14)$$

$$= \frac{T_{\text{sys}}}{\sqrt{B}} \sqrt{\left(\frac{1}{t_{\text{cell}}^{\text{ON}}} + \frac{1}{t_{\text{cell}}^{\text{OFF}}} \right) \times}$$

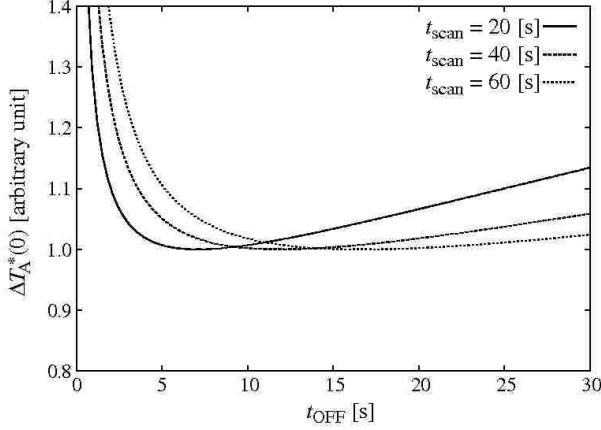


Fig. 3. Dependence of $\Delta T_A^*(0)$ (normalized by the minimum) on t_{OFF} are shown in three cases: $t_{\text{scan}} = 20$ (solid), 40 (dashed), and 60 (dotted) seconds. Common parameters are: $l_1 = 600$ ['], $\Delta l = 5$ ['], $d = 7.5$ ['], $t_{\text{OH}} = 25$ [s], and $N_{\text{scan}}^{\text{SEQ}} = 1$. Bessel \times Gauss convolution ($\eta = 4.3$) is assumed.

$$\sqrt{\left(t_{\text{scan}} + t_{\text{OH}} + \frac{t_{\text{OFF}}}{N_{\text{scan}}^{\text{SEQ}}}\right) N_{\text{row}} f_{\text{cal}}} \quad (15)$$

and is minimized when t_{OFF} is optimal:

$$\frac{\partial}{\partial t_{\text{OFF}}} \Delta T_A^*(0) = 0 \quad (16)$$

leads to

$$t_{\text{OFF}}^{\text{optimal}} \simeq \sqrt{(t_{\text{scan}} + t_{\text{OH}}) \frac{\eta d t_{\text{scan}}}{l_1}} \sqrt{N_{\text{scan}}^{\text{SEQ}}}. \quad (17)$$

This formula is a generalization of the well-known relation $t_{\text{OFF}} = \sqrt{N} t_{\text{ON}}$ for PSW observations, where N is the number of ONs taken per one OFF. Toward $t_{\text{OH}} \rightarrow 0$, Eq. (17) resolves itself into the \sqrt{N} -relation.

Dependence of $\Delta T_A^*(0)$ on t_{OFF} is plotted in Fig. 3. For cases of $t_{\text{scan}} = 20, 40$, and 60 seconds (other parameters are shown in the caption), $\Delta T_A^*(0)$ is minimized at $t_{\text{OFF}}^{\text{optimal}} = 7, 12$, and 17 seconds, respectively. If t_{OFF} is shorter than the optimal value, $\Delta T_A^*(\text{OFF})$ dominates the map. On the other hand, t_{OFF} longer than $t_{\text{OFF}}^{\text{optimal}}$ is excessive since the noise level of the map is limited by $\Delta T_A^*(\text{ON})$.

Using the above notations, it is quantitatively shown how the observing efficiency improves, by adopting appropriate parameters, compared with PSW observations. The following two factors contribute: (1) The ratio of on-source time to the total time spent, $\eta_{\text{ON/OBS}}$, becomes larger because not only the dead time (antenna slew, etc.) is reduced, but also the OFF integration time is relatively shorter ($t_{\text{OFF}} \ll t_{\text{scan}}$); and (2) In general $t_{\text{cell}}^{\text{ON}} \ll t_{\text{cell}}^{\text{OFF}}$, thus ΔT_A^* nearly equals to $\Delta T_A^*(\text{ON})$ (instead of $\Delta T_A^* \simeq \sqrt{2} \Delta T_A^*(\text{ON})$, which is applicable to PSW observation with $t_{\text{ON}} = t_{\text{OFF}}$). As $t_{\text{OH}} \rightarrow 0$ and $t_{\text{scan}} \rightarrow \infty$, the both factors respectively correspond to reduction of observing time by a factor of 2. Thus OTF is, theoretically, up to 4 times more efficient than PSW. In practice,

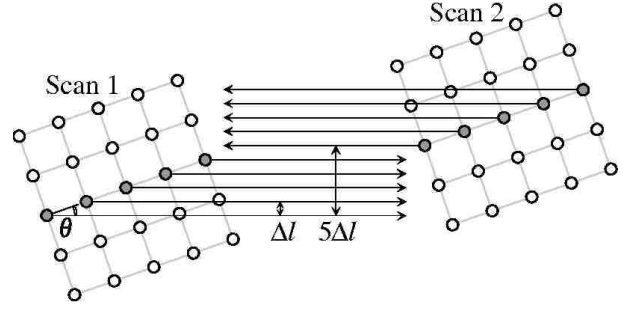


Fig. 4. A schematic illustration of OTF scan patterns with BEARS. The array is inclined by an angle θ with respect to the direction of scans in order to make the scans by neighboring beams separated by Δl . The first scan (labeled as “Scan 1”) and the next (“Scan 2”) are offset by $5\Delta l$ (see text).

improvement of efficiency amounts to a factor of ~ 2 .

4.4. Application to an Array Receiver

The above discussion is made for a single-beam receiver. In case of an array (multi-beam) receiver, some expressions change. Here we consider the case of BEARS, a 5×5 focal plane array.

Fig. 4 schematically shows OTF scans with BEARS considered here. The array is inclined with respect to the scan direction by an angle θ : a neighboring couple of beams makes a pair of scans separated by a distance $\Delta l = L \sin \theta$ ($L = 41''.1$ is a beam separation). The next scan runs $5\Delta l$ away, thus the number of scan rows is written as $N_{\text{row}} = l_2 / (5\Delta l) + 1$. In this case scans made by 5 beams in each row of the array fill the mapped region at a separation of Δl . Since the 5 rows of the array respectively cover the map,

$$t_{\text{cell}}^{\text{ON}} = \frac{5\eta t_{\text{scan}} d^2}{l_1 \Delta l} \quad (18)$$

and

$$t_{\text{cell}}^{\text{OFF}} = \frac{5d}{\Delta l} t_{\text{OFF}}. \quad (19)$$

The noise level of the map is obtained by substituting $t_{\text{cell}}^{\text{ON}}$ and $t_{\text{cell}}^{\text{OFF}}$ in Eq. (13) with Eqs. (18) and (19). Following the transformation in the previous subsection, we have

$$t_{\text{OFF}}^{\text{optimal}} = \sqrt{(t_{\text{scan}} + t_{\text{OH}}) \frac{\eta d t_{\text{scan}}}{l_1}} \sqrt{N_{\text{scan}}^{\text{SEQ}}}, \quad (20)$$

the same expression as Eq. (17).

The strategy mentioned above focuses on mapping speed: compared with the case of a single-beam receiver, the mapped region can be covered 5 times faster and the integration becomes 5 times deeper. There may be another strategy, conscious of the uniformity of the map. Using the same parameters as the case of a single-beam receiver (each beam runs at a separation of Δl), the integration simply becomes 25 times deeper in the same observing time. The point is that every scan path is approximately traced by *all* the 25 beams: characteristics of the beams are expected to be averaged out. However

whether this advantage is realized or not depends on the condition, since the system variation may spoil the uniformity if the observing time becomes too long.

5. Data Processing

5.1. Data Reduction

Reduction process of OTF data is done with *NOSTAR* (Nobeyama OTF Software Tools for Analysis and Reduction) developed in NRO. It is designed to run on UNIX or UNIX-like operating systems. Its core functions (baseline subtraction, creating cube FITS from spectra, etc.) are provided as command-line tools written in C/FORTRAN in order to enable batch processing. These command-line tools are wrapped in graphical user interface (GUI) written in the Interactive Data Language (IDL).

A run of observation produces a Raw Data file (see §3). Spectra from all the used spectrometers are contained within it. The first step of data reduction process is to extract the data to the user's working directory. The task, named *Split*, does not simply copy the Raw Data file, but divide it into *Split Raw Data* files according to the spectrometers. Namely, a Raw Data taken with BEARS is split into 25 Split Raw Data files. Accordingly the following process can be separately applied for each Split Raw Data.

Subsequent procedures of data reduction (baseline subtraction, bad data flagging, etc.) are basically the same as those for PSW data, except for large size of the data. The GUI is designed to be batch-oriented, to help users to proceed the reduction process rapidly without being bothered with a large quantity of data. Each process overwrites the Split Raw Data itself in order to avoid running out of space of the working directory.

Finally a map (cube FITS) is made from the processed spectra. An OTF observation (or a series of observations) produces a set of data points which fills the mapped region with spacings smaller than the Nyquist sampling rate, as described in §4. The data are convolved into the map using a GCF. Desired characteristics of GCFs and appropriate function forms are discussed below. The obtained map may suffer from the so-called *scanning noise* along the scan direction, in addition to the statistical noise. The scanning noise can be effectively removed by combining two maps made from orthogonal scans using the so-called *basket-weave* method. We have implemented the *PLAIT* algorithm described by Emerson & Gräve (1988).

5.2. Gridding Convolution Functions

GCFs used to make maps are desired to have the following characteristics.

First: form of GCF is similar to that of the telescope beam itself. Convolution with such a GCF corresponds to, in the Fourier domain, that a weighting function (Fourier-transformed beam pattern) is multiplied twice to the intrinsic spatial frequency distribution. Consequently the best signal-to-noise ratio is achieved. Though we cannot know the beam pattern at infinite accuracy in practice,

one should choose a GCF so that it mimics the telescope beam.

Second: the GCF's energy concentration ratio is high. In practical convolution operation, the extent of the GCF is finite. Thus, in the Fourier domain, the GCF has artificial frequency components (*sidelobes*). By regridding the data, these sidelobes are folded onto the primary component, resulting in the so-called *aliasing noise*. In order to preserve the observed spatial frequency information, the aliasing effect must be as small as possible. As an index, energy concentration ratio

$$\mathcal{R} = \frac{\int_A |C(\eta)|^2 d\eta}{\int_{-\infty}^{\infty} |C(\eta)|^2 d\eta} \quad (21)$$

is introduced (Briggs, Sramek, & Schwab 1999), where the GCF is $c(l)$, $l = x/\Delta x$, Δx is the grid spacing, $C(\eta)$ is the Fourier transform of $c(l)$, and A is the area in which $\eta < 1$. Here \mathcal{R} represents the degree of concentration of the GCF within A : it is expected that the larger \mathcal{R} is, the smaller the aliasing effect is.

The following GCFs (their shapes are shown in Fig. 5) are implemented so far:

Bessel×Gauss: a Gaussian-tapered Jinc function

$$c(r) = \begin{cases} \frac{J_1(\pi r/a)}{\pi r/a} \exp\left[-\left(\frac{r}{b}\right)^2\right] & (r \leq R_{\max}) \\ 0 & (\text{otherwise}) \end{cases} \quad (22)$$

where J_1 is the 1st-order Bessel function, r is the distance between the data point and the grid point (the unit is the grid spacing). Parameters a , b , and R_{\max} can be arbitrary chosen, and are set as $a = 1.55$, $b = 2.52$, $R_{\max} = 3$ by default (see below).

Sinc×Gauss: a Gaussian-tapered Sinc function

$$c(r) = \begin{cases} \frac{\sin(\pi r/a)}{\pi r/a} \exp\left[-\left(\frac{r}{b}\right)^2\right] & (r \leq R_{\max}) \\ 0 & (\text{otherwise}) \end{cases} \quad (23)$$

The default values for parameters a , b , and R_{\max} are the same as those for the Bessel×Gauss function.

Gauss: a pure Gaussian

$$c(r) = \begin{cases} \exp\left[-\left(\frac{r}{a}\right)^2\right] & (r \leq R_{\max}) \\ 0 & (\text{otherwise}) \end{cases} \quad (24)$$

The default parameters are $a = 1$, $R_{\max} = 3$.

Pillbox: a cell-averaging function

$$c(x, y) = \begin{cases} 1 & (|x| \leq 0.5, |y| \leq 0.5) \\ 0 & (\text{otherwise}) \end{cases} \quad (25)$$

where x and y are the distance between the data point and the grid point (the unit is the grid spacing) in the Cartesian coordinates along the map grid.

Spheroidal: the spheroidal function

$$c(x, y) = \begin{cases} |1 - \eta_x^2|^\alpha \psi_{\alpha 0}(c, \eta_x) \times \\ |1 - \eta_y^2|^\alpha \psi_{\alpha 0}(c, \eta_y) \\ (|\eta_x| \leq 1, |\eta_y| \leq 1) \\ 0 & (\text{otherwise}) \end{cases} \quad (26)$$

where $\eta_x = 2x/m$, $\eta_y = 2y/m$. The parameters $m (= 4, 5, 6, 7, 8)$ and $\alpha (= 0.0, 0.5, 1.0, 1.5, 2.0)$ define the

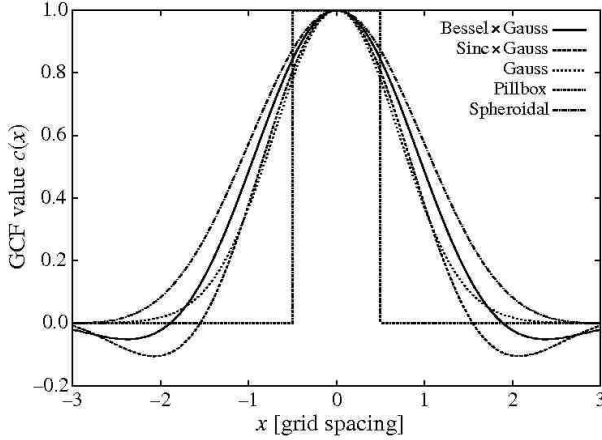


Fig. 5. Shapes of implemented GCFs $c(x)$: Bessel \times Gauss (solid), Sinc \times Gauss (dashed), Gauss (short-dashed), Pillbox (dotted), and Spheroidal (dot-dashed); normalized so that $c(0) = 1$. Function parameters are their default ones (see text).

shape of the function. See Schwab (1984) for details. The defaults are $m = 6$ and $\alpha = 1.0$.

The first four GCFs (Bessel \times Gauss, Sinc \times Gauss, Gauss, and Pillbox) are taken from Mangum, Emerson, & Greisen (2007). Given the cut-off radius $R_{\max} = 3$, the default parameters $a = 1.55$, $b = 2.52$ for the Sinc \times Gauss function are derived so that the energy concentration ratio \mathcal{R} becomes the maximum (Schwab 1984). Using the same parameters, \mathcal{R} does not become the very maximum for the Bessel \times Gauss function (the maximum is found at $a \simeq 1.4$, $b \simeq 2.7$), but is still high enough.

The spheroidal function is taken from Schwab (1984), and is often used to regrid the interferometric visibility (u - v) data. The function form is derived so that \mathcal{R} becomes as high as possible.

As a result of convolution, spatial resolution of the map becomes lower than the telescope beam. We estimate the influence of the beam broadening by calculating the response to a point source. Fig. 6 shows the peak temperature and full-width at half-maximum (FWHM) of the source (i.e., effective beam) on the obtained map, as functions of the grid spacing d . If d is too small, effective integration time for a grid ($t_{\text{cell}}^{\text{ON}}$) becomes small, which leads to a large noise level. In this case the map is too much oversampled, since the spatial resolution is limited by the telescope beam. On the other hand, if d is too large, the effective beam broadens to $\simeq 2d$.

6. Verification

6.1. Performance of the Antennas

In §2, we introduced two parameters t_{app} and t_{tran} , which are duration of “approach-run” and “transit-run”, respectively. They depend on the driving speed and performance of the antenna. In this subsection we describe the measurements to determine t_{app} and t_{tran} . The amount of pointing jitter (PROG – REAL) is also measured.

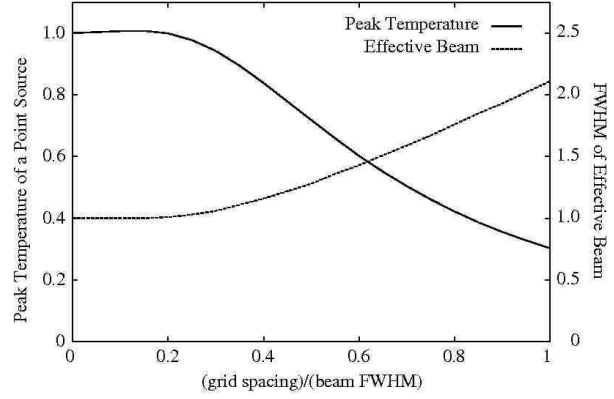


Fig. 6. Dependence of peak temperature of a point source (left-hand axis) and FWHM of effective beam (right-hand axis) on the grid spacing. Beam smearing effect is neglected. The vertical axes are normalized by the original (no convolution) values. The telescope beam is assumed to be a pure Gaussian, and the Bessel \times Gauss convolution with default parameters $a = 1.55$, $b = 2.52$, and $R_{\max} = 3$ is used.

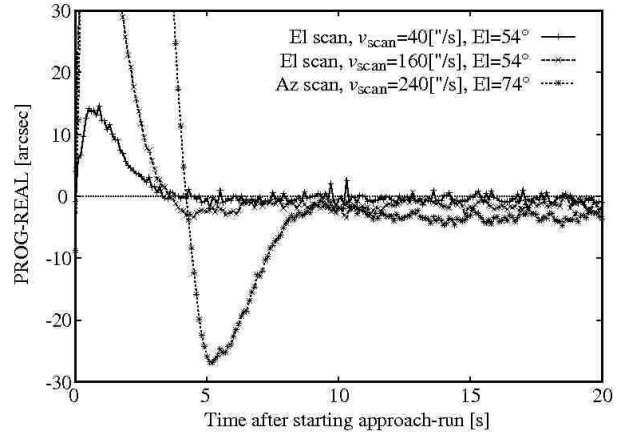


Fig. 7. The PROG – REAL difference of the 45-m telescope along the scan direction on the sky is shown against the time elapsed after starting the approach-run. The measurements were done at every 0.1 second.

6.1.1. NRO 45-m

First, we made scans along both Azimuth (Az) and Elevation (El) at various scan speed v_{scan} , in order to determine t_{app} . The driving speed of the antenna is $v_{\text{scan}}/\cos(\text{El})$ for Az scans, and v_{scan} for El scans. Fig. 7 shows some examples. The PROG – REAL difference on the sky is plotted against the time elapsed after starting the approach-run for three cases (a) El scan with $v_{\text{scan}} = 40$ ["/s] at El = 54°; (b) El scan with $v_{\text{scan}} = 160$ ["/s] at El = 54°; and (c) Az scan with $v_{\text{scan}} = 240$ ["/s] at El = 74° (the driving speed is 870"/s along Az). The case (a) represents the typical scan at 115 GHz, while the case (c) corresponds to the maximum scan speed at 22 GHz. The antenna runs stably after the initial delay and (for large driving speed) an overshoot. The time spent until the stable run begins is adopted to be t_{app} . Determined t_{app} for the three cases are, respectively, 5, 7, and 11 seconds.

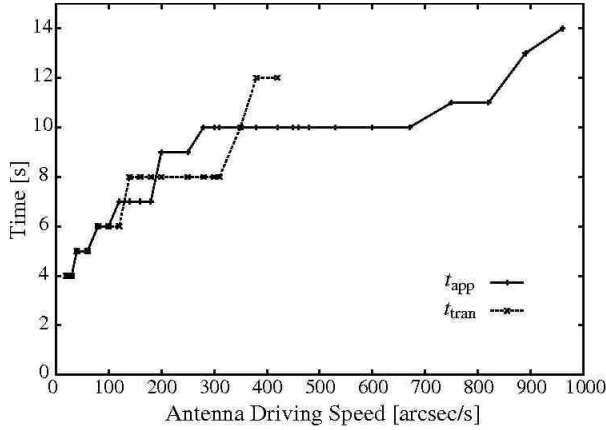


Fig. 8. Derived t_{app} and t_{tran} for the 45-m telescope. The horizontal axis shows the driving speed, $v_{scan}/\cos(\text{El})$ for Az scans and v_{scan} for El scans.

Secondly, t_{tran} is determined in a similar way as t_{app} : back-and-forth scans along Az and El are made using appropriate t_{app} . Various t_{tran} are tried. The optimal t_{tran} is defined as the shortest one for which the antenna starts to move stably after the next approach-run. Fig. 8 shows derived t_{app} and t_{tran} . The both of them monotonically increase with the driving speed. A slight jump of t_{app} is found at the driving speed of $\simeq 200$ ["/s]. It is due to “slow-start slow-stop” control of the telescope, which is implemented not to give sudden and large acceleration to the antenna.

It is found that the PROG – REAL value does not converge into 0 when the driving speed is large (see Fig. 7). Instead, PROG – REAL offset becomes almost constant, which amounts to $|\text{PROG} - \text{REAL}| \simeq 0.016 [\text{s}] \times v_{scan}$. The offset does not affect the observations, since it is about 1/6 of the sampling separation along the scan for t_{dump} of 0.1 second. Excepting the offset, the jitter of the antenna pointing is within a few arcseconds. The error of the sampling separation is determined by the differential of the jitter between the neighboring sample, which is almost within $1''$ – $2''$.

6.1.2. ASTE 10-m

For the ASTE 10-m telescope, t_{app} , t_{tran} , and the pointing jitter are measured in a similar way as the 45-m. The t_{app} measurements for the cases (a) El scan with $v_{scan} = 50$ ["/s] at $\text{El} = 30^\circ$ and (b) Az scan with $v_{scan} = 100$ ["/s] at $\text{El} = 70^\circ$ (the driving speed is $290''/\text{s}$ along Az) are shown in Fig. 9. The case (b) corresponds to the maximum scan speed at 350 GHz. The PROG – REAL values converge into $\simeq 0$ in a few seconds, with jitters of $\lesssim \pm 1''$. From this result, we adopted 4 seconds as t_{app} . The t_{tran} is also measured: for practical observing parameters, 2 seconds are enough. If receivers for higher frequency is installed in the future, the antenna performance should be measured again.

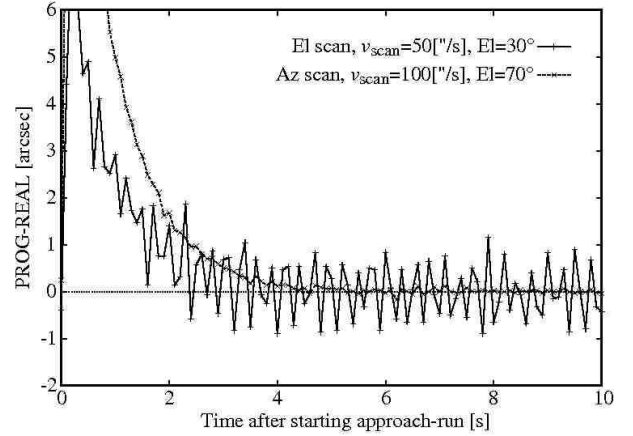


Fig. 9. Same as Fig. 7, but for the 10-m telescope.

6.2. Comparison with PSW Map

In order to confirm the validity and efficiency of OTF observations, the same field has been observed with both OTF and PSW, and the resultant maps are compared. Here we describe ASTE CO $J = 3 - 2$ (345.8 GHz) test observations toward a field centered at $(l, b) = (37^\circ 45', -0^\circ 12')$.

The observations were made in 2005 August and September, as a part of a CO $J = 3 - 2$ Galactic plane survey (Sawada et al., in preparation). The frontend was a cooled SIS mixer receiver, SC345. The system noise temperature was typically 200–300 K in double sideband (DSB) during the observations. The HPBW of the telescope at 350 GHz was measured to be $22''$. The main beam efficiency was ≈ 0.6 . The backend was a 1024-channel MAC, which covers an instantaneous bandwidth of 512 MHz (440 km s^{-1}) with a spectral resolution of 1.0 MHz (0.87 km s^{-1}). The pointing of the telescope was calibrated by tracking a compact CO source W Aql in every 1 or 2 hours, and was within the accuracy of $5''$. We performed intensity calibration by observing a standard source, M17 SW, in every 2 hours. The reproducibility of T_A^* was 5% (1σ). By comparing the observed spectra with those measured with the Caltech Submillimeter Observatory (CSO) 10.4-m telescope with a single-sideband (SSB) filter (Wang et al. 1994), we obtained scaling factors to convert ASTE $T_A^*(\text{DSB})$ into CSO $T_A^*(\text{SSB})$. Hereafter T_A^* is shown in SSB scale.

The OTF observations were carried out with parameters $v_{scan} = 50''/\text{s}$ and $\Delta l = 8''$. Two longitudinal scans and two latitudinal scans (in the Galactic coordinates) were made. We made a map, whose grid spacing is $8'' \times 8'' \times 1 \text{ km s}^{-1}$, using the Bessel \times Gauss convolution; and then the map was resampled onto a $10'' \times 10''$ grid to match the PSW data. A small portion of the region was observed with PSW: 9×9 points separated by $10''$. For each point 10-second integration was made twice. We have convolved the PSW data to make a map having the same resolution ($25''$) and grid spacing as the OTF map. Since the convolution is highly incomplete at the outermost grid

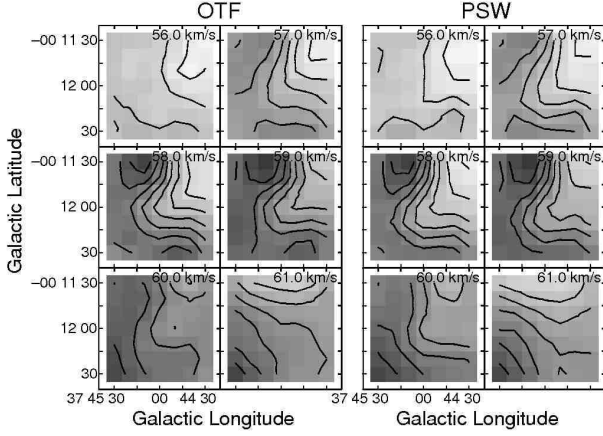


Fig. 10. Velocity channel maps obtained from OTF (left) and PSW (right) observations. The velocity range of $55.5 \leq v_{\text{LSR}} \leq 61.5 \text{ km s}^{-1}$ is sliced into $\Delta v = 1 \text{ km s}^{-1}$ channels. Contours are $T_A^* = 1$ to 9 K at an interval of 1 K.

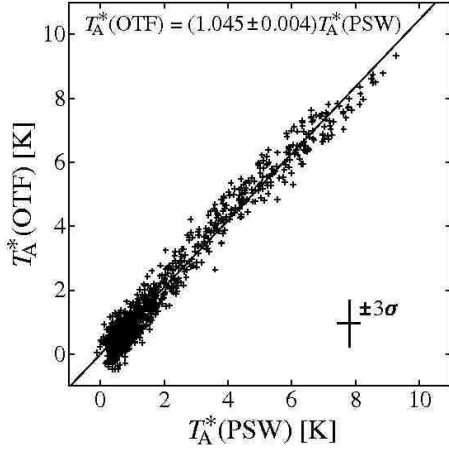


Fig. 11. A correlation plot between PSW and OTF T_A^* in the velocity range $50 \leq v_{\text{LSR}} \leq 70 \text{ km s}^{-1}$. The error of $\pm 3\sigma$ is shown in bottom right. Solid line shows the best fit $T_A^*(\text{OTF}) = (1.045 \pm 0.004) T_A^*(\text{PSW})$.

points, we use the inner 7×7 pixels for comparison.

The 1σ noise levels are 0.25 K (OTF) and 0.12 K (PSW). The obtained OTF noise level agrees with the one derived using the equations in §4, 0.26 K. It is proven that the system has achieved expected observing efficiency. Velocity channel maps of OTF and PSW are shown in Fig. 10. The OTF map is consistent with the PSW one. Fig. 11 shows a pixel-to-pixel correlation plot between them. A least-square fit gives the correlation $T_A^*(\text{OTF}) = (1.045 \pm 0.004) T_A^*(\text{PSW})$. It is confirmed that the OTF map agrees with the PSW map within the accuracy of relative intensity calibration, 5% (reproducibility of the intensity of the standard source).

6.3. FSW Observations

We have implemented FSW observing mode in OTF as described in §3.4.2. As a test of FSW-OTF observations,

IRAS 04369+2539 (IC 2087) in Taurus molecular cloud was observed. High-velocity wing (outflow) emission was found around the source in the $^{12}\text{CO } J=1-0$ line (Heyer et al. 1987). Mapping wing emission in widespread molecular cloud is a presumable science case for FSW observations. Stable spectral baseline is required.

Observations were carried out with the 45-m telescope and BEARS. The HPBW is $15''$, and the system noise temperature was typically 350 K (DSB). The MAC was used in high-resolution mode, i.e., having 32 MHz (83 km s^{-1}) instantaneous bandwidth and 63 kHz (0.16 km s^{-1}) resolution. The OFFs are taken at starting point of approach-runs in order to reduce dead time to slew the antenna. The frequency throw of the LO, $\Delta\nu_{\text{LO}}$, was set to 12 MHz (corresponding to 31 km s^{-1}). The $T_A^*(\text{DSB})$ was converted into $T_A^*(\text{SSB})$ by comparing spectra of a standard source measured with BEARS and an SSB receiver, S100. Linear baselines were subtracted, and a $7''5$ -grid map was made using the Bessel \times Gauss convolution.

Fig. 12 shows a set of velocity channel maps. Redshifted wing emission toward north-south direction is successfully detected beyond the ambient cloud velocity, $v_{\text{LSR}} \simeq 6 \text{ km s}^{-1}$. Fig. 13 shows line profiles at two positions $(\Delta\alpha, \Delta\delta) = (-4', +6')$ and $(-4', -1')$. At $(-4', +6')$, wing emission extending to $\simeq 14 \text{ km s}^{-1}$ is seen, which is consistent with Heyer's results. On the other hand the profile at $(-4', -1')$, which sharply truncates at $\simeq 9 \text{ km s}^{-1}$, demonstrates a straight baseline in a velocity range of 40 km s^{-1} .

6.4. Application to Weak/Broad Line Objects

In general, OTF is effective in particular when widely distributed and intense line is mapped, since a beam runs across a map grid within very short duration, typically $(\text{a few} - 10) \times 0.1$ seconds, without any overhead to point discrete positions. However, application to relatively small-field (\sim a few arcminutes square), weak-and/or broad-line (\sim several 10 mK, several 100 km s^{-1}) sources (e.g., external galaxies) has been successful. For example, Hirota et al. (2008, to be submitted in this volume) observed a galaxy IC 342 using the NRO 45-m and BEARS, and achieved 8 mK rms in T_A^* at a velocity resolution of 5 km s^{-1} .

7. Summary

We have made spectral line OTF observations available at NRO 45-m and ASTE 10-m telescopes. Digital autocorrelation spectrometers can be operated in OTF mode (the data sampling interval is as fast as 0.1 second) with heterodyne receivers mounted on the telescopes, including the 25-beam array receiver, BEARS. Improvements of the software and instruments to enable fast and synchronized controls (e.g., antenna driving, data acquisition, Doppler tracking, frequency switching) were described. Sensitivity of the obtained map was expressed using observing parameters, and we showed how to determine and optimize the parameters. Performance of the antennas was measured and was proven to be high enough for up to 115

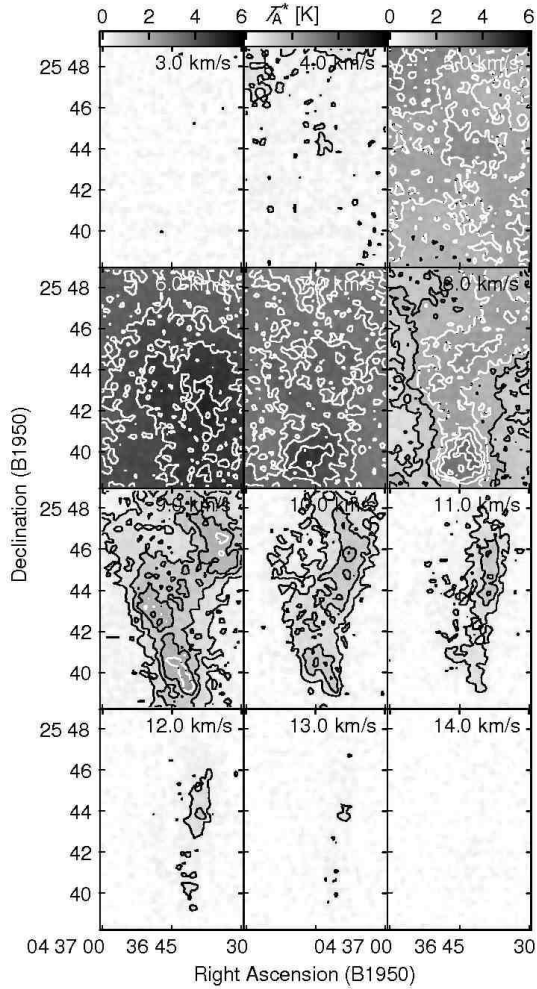


Fig. 12. Velocity channel maps of IC 2087 $^{12}\text{CO } J = 1-0$ emission at an interval of 1 km s^{-1} . Contour levels are $T_A^* = 0.5, 1.0, 1.5, \dots, 5 \text{ K}$.

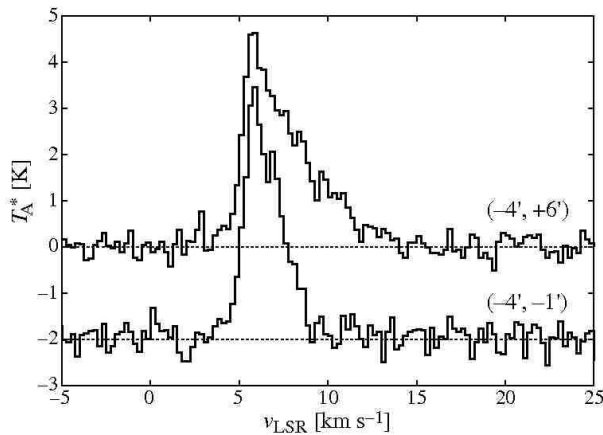


Fig. 13. The CO $J = 1-0$ line profiles at two positions $(\Delta\alpha, \Delta\delta) = (-4', +6')$ [top] and $(-4', -1')$ [bottom, -2 K offset]. The positions are relative to $(\alpha, \delta)_{1950} = (4^{\text{h}}36^{\text{m}}54^{\text{s}}.6, 25^{\circ}39'17'')$

GHz (45-m) or 350 GHz (10-m) observations. The OTF system has improved observing efficiency by a factor of $\simeq 2$ compared with PSW: its mapping capability opens a prospect in various fields of study.

We thank NRO staffs and the ASTE team members for their support. In particular, we acknowledge Satoshi Hongo, Aya Higuchi, Rie Miura, Nobuyuki Yamaguchi, and Kunihiko Tanaka for their contribution to development and evaluation.

References

- Briggs, D. S., Sramek, R. A., & Schwab, F. R. 1999, ASP Conf. Ser. 180, Synthesis Imaging in Radio Astronomy II, 127
- Emerson, D. T., & Gräve, R. 1988, A&A, 190, 353
- Ezawa, H., Kawabe, R., Kohno, K., & Yamamoto, S. 2004, Proc. SPIE, 5489, 763
- Heyer, M. H., Snell, R. L., Goldsmith, P. F., & Myers, P. C. 1987, ApJ, 321, 370
- Ikeda, N., Sunada, K., & Kitamura, Y. 2007, ApJ, 665, 1194
- Kamazaki, T., et al. 2005, ASP Conf. Ser. 347, Astronomical Data Analysis Software and Systems XIV (San Francisco: ASP), 533
- Kohno, K. 2005, in ASP Conf. Ser. 344, The Cool Universe: Observing Cosmic Dawn (San Francisco: ASP), 242
- Mangum, J. G., Emerson, D. T., & Greisen, E. W. 2000, in ASP Conf. Ser. 217, Imaging at Radio through Submillimeter Wavelengths (San Francisco: ASP), 179
- Mangum, J. G., Emerson, D. T., & Greisen, E. W. 2007, A&A, 474, 679
- Morita, K.-I., Nakai, N., Takahashi, T., Miyazawa, K., Ohishi, M., Tsutsumi, T., Takakuwa, S., Ohta, H., & Yanagisawa, K. 2003, in ASP Conf. Ser., Vol. 295, ADASS XII, ed. H. E. Payne, R. I. Jedrzejewski, & R. N. Hook (San Francisco: ASP), 166
- Muders, D., Peters, W. L., Butner, H. M., Gensheimer, P. D., Wilson, T. L., Uchida, K. I., Kramer, C., & Tieftrunk, A. R. 2000, in ASP Conf. Ser. 217, Imaging at Radio through Submillimeter Wavelengths (San Francisco: ASP), 203
- Penzias, A. A., & Burrus, C. A. 1973, ARA&A, 11, 51
- Schwab, F. R. 1984, in Indirect Imaging, ed. J. A. Roberts (Cambridge: Cambridge University Press), 333
- Sorai, K., Sunada, K., Okumura, S. K., Iwasa, T., Tanaka, A., Natori, K., & Onuki, H. 2000, in Proc. SPIE, 4015, 86
- Sunada, K., Yamaguchi, C., Nakai, N., Sorai, K., Okumura, S. K., & Ukita, N. 2000, in Proc. SPIE, 4015, 237
- Ulich, B. L., & Haas, R. W. 1976, ApJS, 30, 247
- Ungerechts, H., Brunswig, W., Kramer, C., Paubert, G., Sievers, A., & Wild, W. 2000, in ASP Conf. Ser. 217, Imaging at Radio through Submillimeter Wavelengths (San Francisco: ASP), 190
- Wang, Y., Jaffe, D. T., Graf, U. U., & Evans, N. J., II. 1994, ApJS, 95, 503
- Yamaguchi, C., Sunada, K., Iizuka, Y., Iwashita, H., & Noguchi, T. 2000, in Proc. SPIE, 4015, 614